J. Fluid Mech. (1998), *vol.* 358, *pp.* 61–85. Printed in the United Kingdom

Direct numerical simulation of a three-dimensional temporal mixing layer with particle dispersion

By WEI LING, J. N. CHUNG, T. R. TROUTT AND C. T. CROWE

School of Mechanical and Materials Engineering, Washington State University, Pullman, WA 99164, USA

(Received 20 December 1996 and in revised form 21 July 1997)

The three-dimensional mixing layer is characterized by both two-dimensional and streamwise large-scale structures. Understanding the effects of those large-scale structures on the dispersion of particles is very important. Using a pseudospectral method, the large-scale structures of a three-dimensional temporally developing mixing layer and the associated dispersion patterns of particles were simulated. The Fourier expansion was used for spatial derivatives due to the periodic boundary conditions in the streamwise and the spanwise directions and the free-slip boundary condition in the transverse direction. A second-order Adam–Bashforth scheme was used in the time integration. Both a two-dimensional perturbation, which was based on the unstable wavenumbers of the streamwise direction, and a three-dimensional perturbation, derived from an isotropic energy spectrum, were imposed initially. Particles with different Stokes numbers were traced by the Lagrangian approach based on one-way coupling between the continuous and the dispersed phases.

The time scale and length scale for the pairing were found to be twice those for the rollup. The streamwise large-scale structures develop from the initial perturbation and the most unstable wavelength in the spanwise direction was found to be about two thirds of that in the streamwise direction. The pairing of the spanwise vortices was also found to have a suppressing effect on the development of the three-dimensionality. Particles with Stokes number of the order of unity were found to have the largest concentration on the circumference of the two-dimensional large-scale structures. The presence of the streamwise large-scale structures causes the variation of the particle concentrations along the spanwise and the transverse directions. The extent of variation also increases with the development of the three-dimensionality, which results in the 'mushroom' shape of the particle distribution.

1. Introduction

Understanding the mechanism of particle dispersion in turbulent free shear flows is important in many industrial, environmental and energy-related processes. The two-dimensional mixing layer has been extensively studied over the past twenty years (Ho & Huerre 1984). The associated large-scale organized spanwise vortex structures have been identified and studied both numerically and experimentally. Extensive numerical and experimental studies have also been carried out to examine particle dispersion by organized vortex structures. The large structures have a dominant effect on the

dispersion of particles over a range of Stokes numbers (Eaton & Fessler 1994; Crowe, Chung & Troutt 1988, 1996).

Although the two-dimensional large vortex structures are very stable, many experiments (Miksad 1972; Breidenthal 1978; Browand & Troutt 1980) have shown that they are still subject to three-dimensional instabilities. The scale of three-dimensional instabilities, which cause the streamwise streaks and contortion of the two-dimensional rollers, was found to be smaller than that of two-dimensional instabilities (Wygnanski *et al.* 1979). The reason for the deformations or corrugations of the two-dimensional large vortex structures may be due to the presence of the 'transversally' oriented vortices (Breidenthal 1981). The location of the transition to three-dimensionality for the plane mixing layer varies depending on the magnitude and location of the upstream perturbations. However, the streamwise vortices were always first found on the braids between the spanwise vortices (Lasheras, Cho & Maxworthy 1986). While the developments of two-dimensional instability and three-dimensional instability are almost uncoupled during the formation of the streamwise vortex tubes, once the vortex tubes form, they undergo nonlinear interactions with the spanwise vortices and induce, on the spanwise vortex cores, a wary undulation of the same wavelength and a phase shift of 180° with respect to the perturbation (Lasheras & Choi 1988). The wavelengths of the spanwise vortex structures and the streamwise vortices increase as the spanwise vortices merge, but the ratio of the two length scales was found to be a constant (Huang & Ho 1990).

The three-dimensionality of the plane mixing layer has been observed and studied not only in experiments but also in numerical simulations. The counter-rotating 'rib' vortices, which are due to the three-dimensional instability of the mixing layer and exist in the region between the rollers (the braid region) and extend from the bottom of one roller to the top of the next one, were also found in most numerical simulations. The wavelength of the three-dimensional instability was found to be about two thirds of the wavelength of the two-dimensional instability (Pierrehumbert & Widnall 1982). The small-scale three-dimensional instabilities were shown to exist in free shear flows at moderately low Reynolds numbers, and are responsible for the initial development of the three-dimensionality. And the pairing of the two-dimensional large-scale vortex structures has a suppressing effect on the growth rate of the three-dimensional structures. Once the three-dimensional modes reach a finite amplitude, they manifest themselves mainly as counter-rotating, streamwise vortices that locate on the braids between the spanwise coherent two-dimensional paring modes and the stabilizing effect of the two-dimensional structures is reduced (Metcalfe *et al.* 1987; Moser & Rogers 1993).

Owing to the improvement of computer techniques, direct numerical simulation is becoming a very powerful tool to obtain three-dimensional, time-dependent solutions to the nonlinear Navier–Stokes equations. Spectral methods have been proven to be the prevailing numerical method for large-scale computations of transitional and turbulent flows owing to the very high accuracy in space and fast convergence. However, broad applications of the method are still limited by finite computer resources and this limitation restricts the simulations to flows with moderate Reynolds numbers and fairly simple geometries. Spectral method and finite-difference schemes were used to simulate particle dispersion in decaying isotropic and homogeneous turbulence (Elghohashi 1994). The pseudospectral method was also employed to simulate particle dispersion in homogeneous and isotropic turbulence by Yeung & Pope (1988), Squires & Eaton (1990, 1991*a–c*) and Wang & Maxey (1993).

Marcu & Meiburg (1996*a–c*) initiated an investigation on the effect of streamwise

vortices on the dispersion of particles in a plane mixing layer both in the absence and in the presence of gravity. The equilibrium points and nonlinear dynamics of small heavy spherical particles in a steady quasi-two-dimensional flow were studied first. It was found that only the particles with very small Stokes numbers can accumulate at the streamwise vortex centres. Particles with moderate Stokes numbers smaller than a critical value which depends on the dimensionless strain rate and gravity parameter, tend to orbit around individual streamwise vortices. The features of particle dispersion in a three-dimensional temporal plane mixing layer were then investigated without vortex pairing. The presense of the streamwise vortices results in additional dynamical effects that modify the dispersion patterns of particles. Intense three-dimensional vortex stretching and folding produces 'mushroom' shapes of particle dispersion patterns.

The object of the present work is to investigate the three-dimensional dispersion patterns of different sized particles in a temporal mixing layer by including vortex pairing in the development of the flow and using non-forcing three-dimensional perturbations. Two two-dimensional and two three-dimensional flow cases were simulated first to ensure the flow field was behaving correctly. Three-dimensional dispersion patterns of particles with different Stokes numbers were then examined.

2. Numerical approach

The flow field simulated here is a temporally developing mixing layer. The requirement of specifying inflow–outflow-boundary conditions, which is inevitable in simulations of a spatially growing flow, are avoided. Because the spatially periodic boundary conditions in the streamwise and spanwise directions can be used for the temporally developing flow, a more efficient and accurate program can be written and implemented using the pseudospectral method. In the transverse direction, as long as the size of the computational domain is large enough, the free-slip boundary condition can be used.

2.1. *Basic equations*

2.1.1. *Flow field simulation*

The non-dimensional continuity and momentum equations for an incompressible flow with no body force are:

$$\nabla \cdot \boldsymbol{U} = 0, \tag{2.1}$$

$$\frac{\partial \boldsymbol{U}}{\partial t} = -\nabla P + \frac{1}{Re}\nabla^2 \boldsymbol{U} - \boldsymbol{U} \cdot \nabla \boldsymbol{U}. \tag{2.2}$$

The equations are non-dimensionalized by U_0, the velocity difference between the two parallel free streams, the density of the flow and L_0, a length scale. The length scale is so chosen that the dimensions of the non-dimensional computational domain are integral multiples of 2π and the size of the domain must be an integral multiple of the most unstable wavelength. Given λ_x as the most unstable streamwise wavelength, the length scale L_0 should be equal to $\lambda_x/2\pi$. However, λ_x is determined by the initial vorticity thickness which depends on the initial mean velocity profile. In the present simulation, the sizes of the computational domain in the three directions are all chosen to be 4π.

2.1.2. *Particle dispersion*

If the mass loading ratio is on the order of unity, the particle volume fraction will be of the order of 10^{-3} for most gas–particle flows. In such a flow, the particle collision can be neglected (Ishii, Umeda & Yuhi 1989). In the present simulation, the mass loadings for most particle-dispersion cases are of the order of unity or less, so the flow can be treated as dilute. Therefore, we have the following assumptions concerning the motion analysis of particles.

(i) All particles are rigid spheres with identical diameter d_p and density ρ_p.
(ii) The density of particles is much larger than that of the fluid.
(iii) Particle–particle interactions are neglected.
(iv) Gravity effect on particles is neglected.
(v) Initially, the particles are distributed uniformly and are in dynamic equilibrium with the fluid.

With the above assumptions, the non-dimensional motion equation for a particle is

$$\frac{\mathrm{d}\boldsymbol{V}}{dt} = \frac{f}{St}(\boldsymbol{U} - \boldsymbol{V}) \tag{2.3}$$

where $\boldsymbol{V}$ is the velocity of a particle, $\boldsymbol{U}$ is the velocity of fluid at the position of the particle and f is the modification factor for the Stokes drag coefficient. As long as the particle's Reynolds number Re_p, which is defined as $|\boldsymbol{U} - \boldsymbol{V}|d_p/v$, is less than 1000, the factor f is well represented by $f = 1 + 0.15Re_p^{0.687}$. St is the Stokes number of particle, which is defined as the ratio of the particle's momentum response time to the flow field time scale:

$$St = \frac{\rho_p d_p^2/18\mu}{L_0/U_0}. \tag{2.4}$$

The velocity and position of a particle can be obtained by integrating (2.3):

$$\boldsymbol{V}^{n+1} = \boldsymbol{U} + (\boldsymbol{V}^n - \boldsymbol{U})\mathrm{e}^{-f\Delta t/St}, \tag{2.5}$$

$$\boldsymbol{X}_p^{n+1} = \boldsymbol{X}_p^n + \boldsymbol{U}\Delta t + (\boldsymbol{V}^n - \boldsymbol{U})\frac{St}{f}(1 - \mathrm{e}^{-f\Delta t/St}), \tag{2.6}$$

where the fluid velocity $\boldsymbol{U}$ and f are taken as constants during the integration.

Because one only has the velocity of the flow field at every grid point, the third Lagrange interpolating polynomial is used to obtain the flow velocities at the positions of particles.

2.2. *Numerical considerations*

2.2.1. *Initial flow field*

The initialization of the flow velocity field consists of two parts. One is the mean velocity field and the other is the perturbations to the mean. Since a temporal mixing layer is simulated, the initial mean velocity field is given as a function of the transverse direction only and the hyperbolic tangent profile (figure 1) is used here:

$$U(y) = \tfrac{1}{2}U_0 \tanh(y/\delta) \tag{2.7}$$

Two different perturbations are used in the present simulation. The first part is the initial two-dimensional perturbation, which is imposed on the two-dimensional fundamental and subharmonic unstable wavenumbers, derived from the linear Orr–Sommerfeld equations (Michalke 1964). It is used to initialize the two-dimensional simulations and added to all three-dimensional simulations. The second part is the

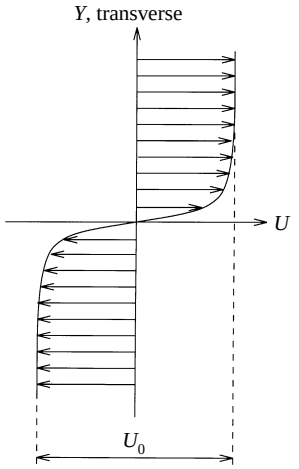

FIGURE 1. Initial mean velocity profile

initial three-dimensional perturbation which is a specific energy spectrum with random fluctuating components. The initialization procedure is similar to that used by McMurtry, Riley & Metcalfe (1989) (see the Appendix).

2.2.2. *Numerical procedure*

The problem with the numerical algorithm for equations (2.1) and (2.2) is the absence of an evolution equation for the pressure. The pressure changes, however, as the velocity evolves in time so the flow field remains non-divergent. An explicit, fractional time step method, which is similar to the so called 'projection method' for incompressible unsteady Navier–Stokes equations (Peyret & Taylor 1983), is used in the present simulation. All spatial derivatives are computed in spectral space.

First, the second-order Adam–Bashforth scheme is used to advance the velocity field to an intermediate time step without the effect of the pressure gradient:

$$\boldsymbol{U}^{n+1/2} = \boldsymbol{U}^n + \Delta t(\tfrac{3}{2}\boldsymbol{A}^n - \tfrac{1}{2}\boldsymbol{A}^{n-1}) \tag{2.8}$$

where $\boldsymbol{A} = (1/Re)\nabla^2\boldsymbol{U} - \boldsymbol{U}\cdot\nabla\boldsymbol{U}$. Then, at the second step, the $\mathbf{U}^{n+1/2}$ is corrected by considering the pressure effect:

$$\frac{\boldsymbol{U}^{n+1} - \boldsymbol{U}^{n+1/2}}{\Delta t} = -\nabla \boldsymbol{P}^{n+1}. \tag{2.9}$$

Taking divergence of equation (2.9) and using the continuity equation, one obtains the Poisson equation for the pressure:

$$\nabla^2 \boldsymbol{P}^{n+1} = \frac{1}{\Delta t}\nabla\cdot\boldsymbol{U}^{n+1/2}. \tag{2.10}$$

3. Results of flow field simulations

Four flow field simulations were performed as shown in table 1. The case 2D0P has an initial two-dimensional perturbation imposed only on the fundamental unstable wavenumber and the magnitude of the perturbation $A_{(1,0)}$ is 1.0. The case 2D1P has an initial two-dimensional perturbation imposed on both fundamental

Case	$A_{(1,0)}$	$A_{(0.5,0)}$	ε_{3D}
2D0P	1.0	0.0	0.0
2D1P	1.0	1.3	0.0
Low3D	1.0	1.3	0.0005
Pdel	1.0	0.5	0.0005

TABLE 1. Cases of flow field simulation

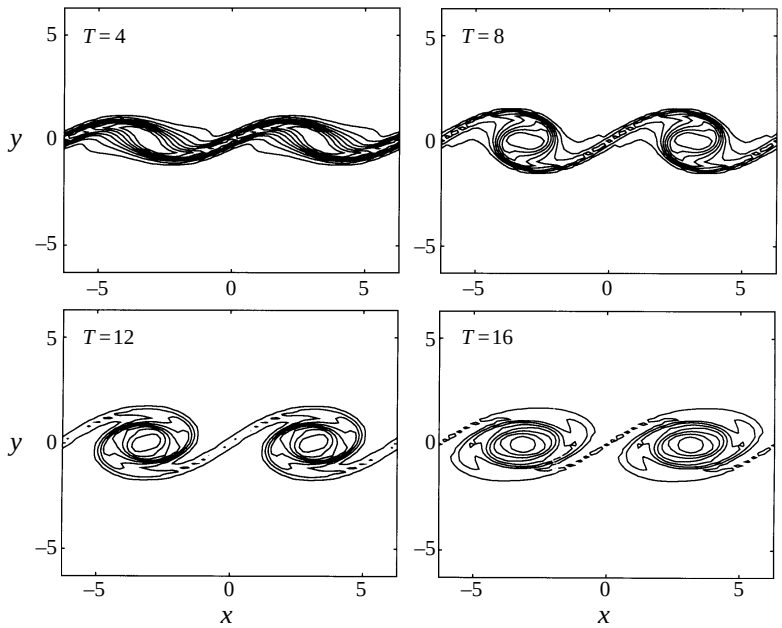

FIGURE 2. Contours of spanwise vorticity at $Z = 0$ for the 2D0P case.

and subharmonic unstable wavenumbers and the magnitude of the perturbation on subharmonic unstable wavenumber $A_{(0.5,0)}$ is 1.3. Low3D is the case where, besides the initial two-dimensional perturbation, an initial three-dimensional perturbation with a low magnitude is imposed on the low wavenumbers and the magnitude of the perturbation ε_{3D} is 0.0005. For the case Pdel a smaller initial perturbation to the subharmonic unstable wavenumber is imposed, compared to the Low3D case. The Reynolds number, which is based on the velocity scale U_0 and the length scale L_0, is 500 for all cases. The computational grids are $65 \times 65 \times 65$.

The magnitudes of the initial two-dimensional perturbations $A_{(1,0)}$ and $A_{(0.5,0)}$ are so chosen, as given in table 1, that the time scales of the rollup and the pairing are of the same order of magnitude as those of Moser & Rogers' normal pairing case (Moser & Rogers 1993). The magnitude of the initial three-dimensional perturbation ε_{3D} was chosen as small as possible but also large enough to produce a three-dimensional fully developed flow in a reasonable time frame.

Because the computational grids are only $65 \times 65 \times 65$, the grid system is not fine enough to resolve all the small scales in the turbulence and the low-resolution problem was encountered. However, as the development of the large-scale structure is the object

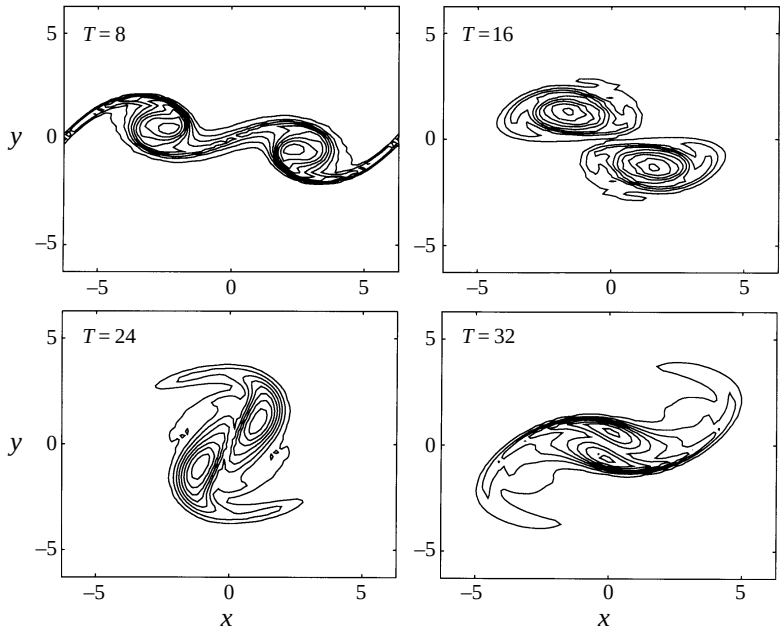

FIGURE 3. Contours of spanwise vorticity at $Z = 0$ for the 2D1P case.

of our simulation, the small structures associated with the high wavenumbers are not of interest. In the meantime, during the development of turbulence, the mean flow energy is first transferred to the largest-scale structure and little energy is contained in the high wavenumbers at that time. This is also why the initial three-dimensional perturbation is only given to the low wavenumbers.

3.1. *Two-dimensional simulations*

Because the two-dimensional features have a large impact on the development of three-dimensionality in the flow, two two-dimensional cases were simulated first. As no initial three-dimensional perturbation was given, although the flow field is three-dimensional, the properties of the flow are unique in the spanwise direction.

The contours of spanwise vorticity for the 2D0P case (figure 2) show that the initial perturbation on the fundamental unstable wavenumber causes the development of the spanwise Kelvin–Helmholtz rollers. The contours of spanwise vorticity for the 2D1P case (figure 3) show that the development of the first pairing of two adjacent Kelvin–Helmholtz rollers, which is caused by the initial perturbation on the subharmonic unstable wavenumber. During the pairing, a pair of well-developed rollers come together, corotate and eventually amalgamate to form a new bigger roller. The spanwise vortices are depleted in the braid region (the region between pairings) while the pairing is occurring. However, after the pairing, the spanwise vortices are advected back into the braid region, which is called oversaturation (Moser & Rogers 1993).

We can define some time scales which are associated with the rollup, pairing and oversaturation (Moser & Rogers 1993). The rollup time, τ_r, is defined as when the energy of the two-dimensional fundamental Fourier modes $E_{(1,0)}$ reaches the first

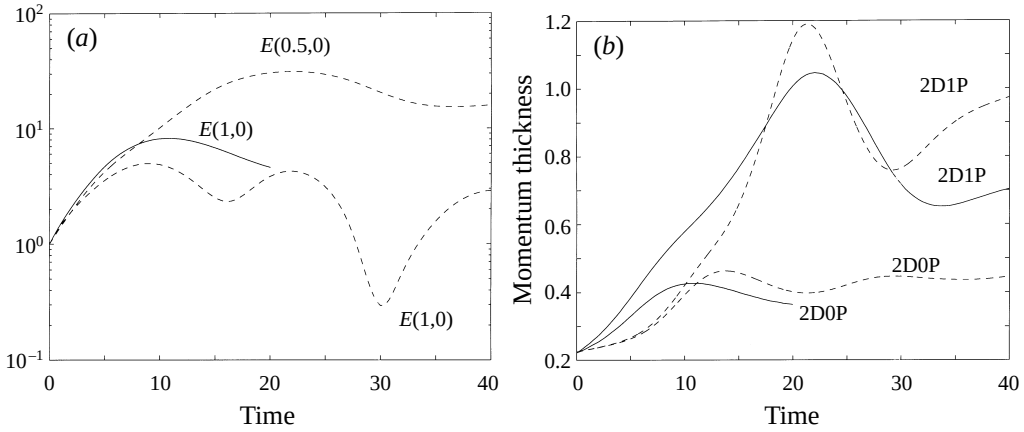

FIGURE 4. Development of (*a*) $E_{(1,0)}$, $E_{(0.5,0)}$ and (*b*) δ_m for the 2D0P and 2D1P cases. (*a*) solid line: 2D0P; dashed line: 2D1P; (*b*) dashed lines: results from Moser & Rogers.

maximum value. $E_{(1,0)}$ is defined as

$$E_{(1,0)} = \sum_{k_y} C_u\Big|_{k_x=1,k_z=0} \tag{3.1}$$

where $C_u = |C_1|^2 + |C_2|^2 + |C_3|^2$, and C_1, C_2, C_3 are the Fourier coefficients of three velocity components U_1, U_2, U_3, respectively.

The pairing time, τ_p, is defined as when the energy of the two-dimensional subharmonic Fourier modes $E_{(0.5,0)}$ reaches the first maximum value. $E_{(0.5,0)}$ is defined as

$$E_{(0.5,0)} = \sum_{k_y} C_u\Big|_{k_x=0.5,k_z=0}. \tag{3.2}$$

From the evolution histories of $E_{(1,0)}$ and $E_{(0.5,0)}$ shown in figure 4, we can tell that the rollup time for case 2D0P is about 10.6, the rollup time for case 2D1P is about 10.8 and the pairing time for case 2D1P is about 21. The rollup time for the two cases are almost the same, and the paring time is about twice the rollup time. We should note that the momentum thickness δ_m also reaches local maximum values around the rollup time and the pairing time as shown in figure 4. The momentum thickness is defined as

$$\delta_m = \int_{-\infty}^{\infty} (0.25 - \overline{U_1(y)}^2)\mathrm{d}y \tag{3.3}$$

where

$$\overline{U_1(y)} = \frac{\displaystyle\int_{-L_x/2}^{L_x/2}\int_{-L_z/2}^{L_z/2} U_1(x,y,z)\mathrm{d}x\mathrm{d}z}{L_x L_z}. \tag{3.4}$$

It should also be noted that for the 2D1P case, the momentum thickness at the pairing time is also about twice that at the rollup time, which means the length scale of pairing is about twice the length scale of rollup. As the time scale of pairing is about twice that of rollup, and the velocity scale remains the same, the length scale should be doubled. The results were also compared with those of Moser & Rogers (1993) in figure 4.

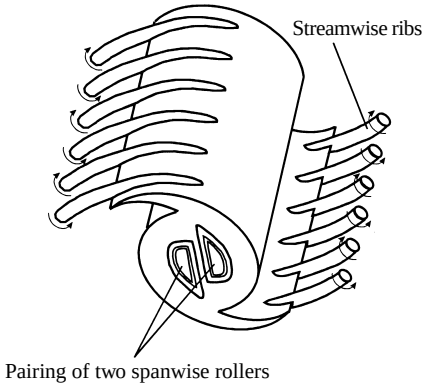

FIGURE 5. Sketch of three-dimensional large structures in the mixing layer.

3.2. *Three-dimensional simulations*

3.2.1. *Three-dimensional structures*

As mentioned previously, the two-dimensional, large-scale structures are subjected to three-dimensional instability which can result in counter-rotating 'rib' vortices. They exist in the braid region and extend from the bottom of one roller to the top of the next. The sketch in figure 5 shows the basic structure of the three-dimensional large-scale structures in the mixing layer.

The three-dimensional large-scale structures in the present simulation can be shown by plotting an iso-surface of ω_a, which is defined as $|\omega_x| + |\omega_y| + |\omega_z|$, as shown in figure 6. The streamwise counter-rotating 'rib' structures can also be shown in the plot of the iso-surface of ω_x for two given values as shown in figure 7. The similarity between figure 6 and figure 5 is apparent. The magnitude of the vorticity is not used because $|\omega_z|$ is much larger than the other two components and the three-dimensional structure is what is concerned. Because the initial three-dimensional perturbation in the present work is more like a natural small disturbance, the three-dimensional large-scale structures develop by themselves from the three-dimensional instability.

One should also note that the streamwise 'rib' structure has three periods which means that the dimensions in the spanwise direction are about three times that of the most unstable wavelength in the spanwise direction λ_z. Because the dimensions in the streamwise direction are twice that of the most unstable wavelength in the streamwise direction λ_x, and the dimensions in the streamwise direction and in the spanwise direction are both 4π, λ_z must be about two thirds of λ_x. This result also complies with the previous study of Pierrehumbert & Widnall (1982).

3.2.2. *Effects of pairing on the development of three-dimensionality*

In the Pdel case, a smaller magnitude initial perturbation on the subharmonic wavenumber in the streamwise direction is given, which causes a delay in pairing. This delay results in a longer pairing time and re-entry time, which can be shown in the development of the momentum thickness δ_m for the Low3D and Pdel cases as shown in figure 8.

To study the development of the three-dimensionality, one must define two properties. The first one, E_{3D}, which represents the total energy in the three-dimensional

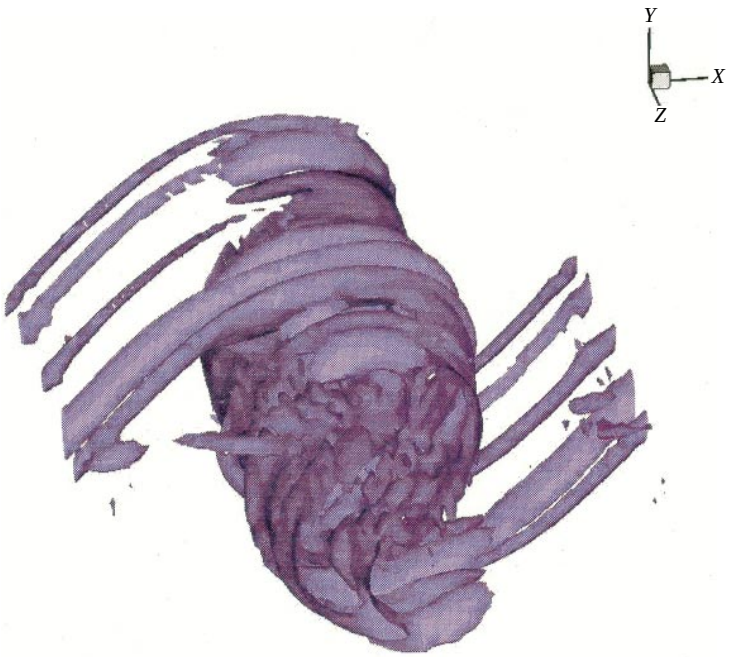

FIGURE 6. Iso-surface of $\omega_a = 0.45$ in grid coordinate. For case Low3D; $T = 24$.

FIGURE 7. Iso-surface of $\omega_x = \pm 0.24$ (blue, positive; green negative) in grid coordinates for case Low3D; $T = 24$.

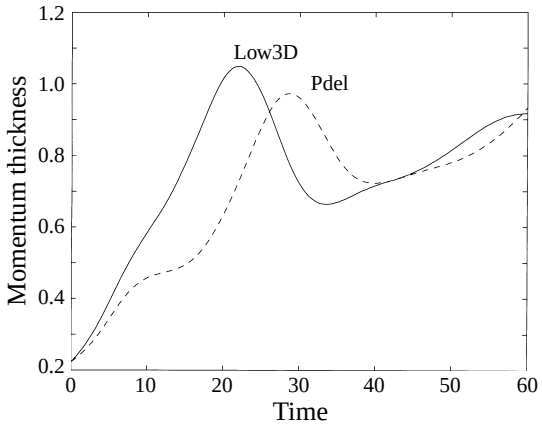

FIGURE 8. Development of δ_m for the Low3D and Pdel cases.

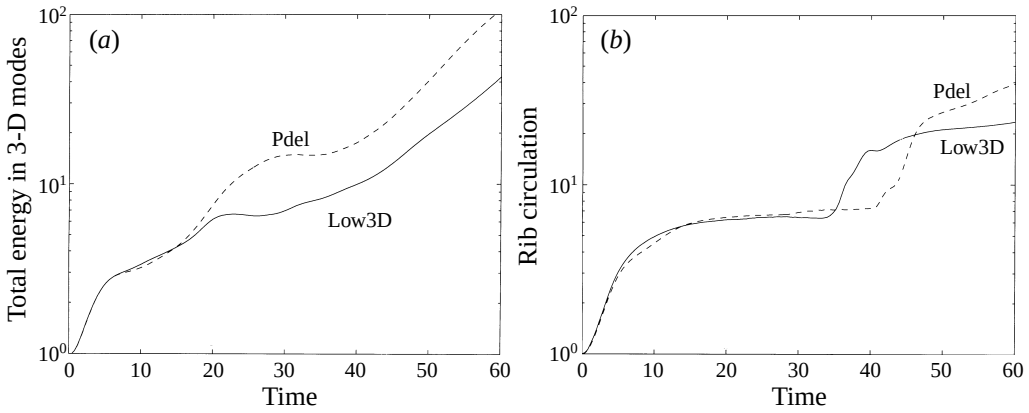

FIGURE 9. Development of (*a*) E_{3D} and (*b*) Γ_x, normalized by the initial values, for the Low3D and Pdel cases.

Fourier modes, is defined as

$$E_{3D} = \sum_{k_x} \sum_{k_y} \sum_{k_z \neq 0} C_u \tag{3.5}$$

where $C_u = |C_1|^2 + |C_2|^2 + |C_3|^2$, and C_1, C_2, C_3 are the Fourier coefficients of the three velocity components U_1, U_2, U_3 respectively.

The other one is the rib circulation Γ_x, which is defined as

$$\Gamma_x = \int_{-\infty}^{\infty} \int_0^{\lambda_z/2} \omega_x \mathrm{d}z \mathrm{d}y \Big|_{MP} \tag{3.6}$$

where MP is the mid-braid plane. The rib circulation can represent the degree of three-dimensionality in the mixing layer (Moser & Rogers 1993).

From the development of E_{3D} and Γ_x as shown in figure 9, one can tell that the development of the three-dimensionality is suppressed during the pairing and that the degree of three-dimensionality in the Pdel case is higher than that in the Low3D case at a later time, which also resulted from the delay in pairing.

Moser & Rogers (1993) also studied the development of the rib circulation for the

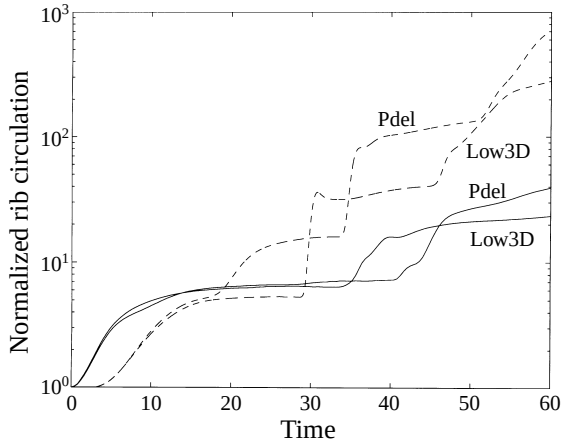

FIGURE 10. Comparison of the development of Γ_x. Dashed lines: results of Moser & Rogers.

normal pairing case and the delayed pairing case. Although only three-dimensional linear perturbations were used in those two cases, the development of the rib circulations for the normal pairing and delayed pairing cases is similar to the Low3D and Pdel cases respectively as shown in figure 10.

Owing to the limit of computer resources, only $65 \times 65 \times 65$ grids was used for most of the present work. However, a three-dimensional flow field simulation case using $129 \times 129 \times 129$ grid system with the same initial conditions as the Low3D case was performed. and some results are compared with those of the $65 \times 65 \times 65$ grid system. Because $65 \times 65 \times 65$ grids are fine enough to resolve the large structures in the mixing layer, the development of the momentum thickness, the energy spectrum on the fundamental and subharmonic unstable wavenumbers, and the development of the spanwise large-scale vortex structures are almost the same for the two cases.

4. Results of particle dispersion

The dispersion of particles at Stokes numbers ranging from 0.001 to 1000 was simulated. The flow field of the 2D1P case was used in the two-dimensional particle dispersion simulation for particles with Stokes number 4 and the flow field of the Low3D case was used in the three-dimensional particle dispersion simulations. Initially, there is one particle at the centre of each computational cell and the velocity of each particle is exactly the same as the fluid velocity at that position. Since there are periodic boundary conditions in the streamwise and the spanwise directions, the particles which move out the box in those two directions from one side will be put back in the box from the other side. The particles which move out the box in the transverse direction will not be taken back.

The root mean square of particle number per cell over the whole field, N_{rms}, is used to determine the overall concentration character of particles. The N_{rms} is obtained from

$$N_{rms} = \left(\sum_{i=1}^{N_c} {N_i}^2 / N_c \right)^{1/2} \tag{4.1}$$

where N_c is total number of computational cells and N_i is the number of particles in the ith cell. It is noted that $N_c = 64 \times 64 \times 64$ and when $T = 0$, $N_{rms} = 1$.

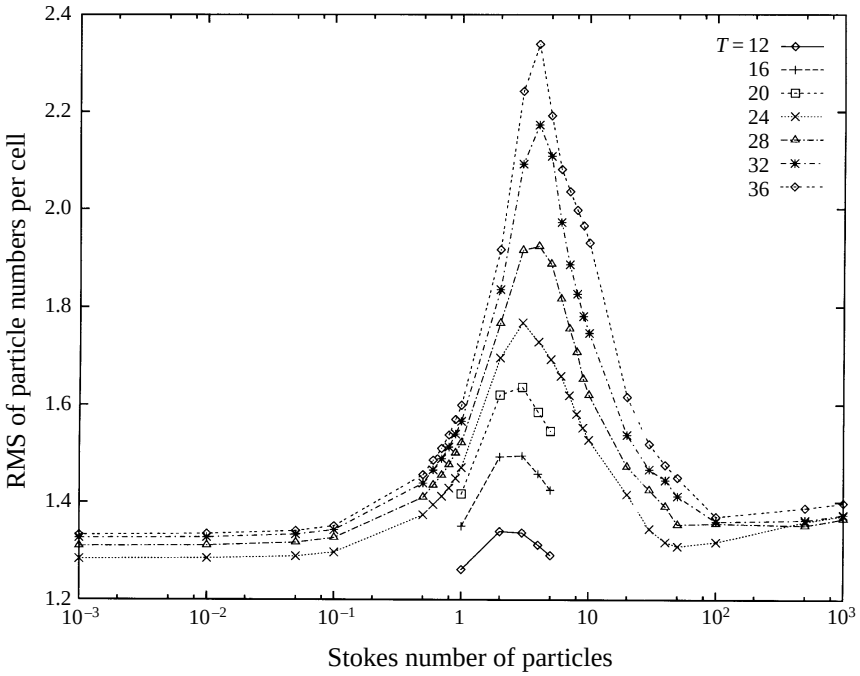

FIGURE 11. N_{rms} for particles at different Stokes number.

N_{rms} for particles with different Stokes numbers at different times is shown in figure 11. It is obvious that the particles with Stokes number of order of unity apparently have larger N_{rms} values and the value of N_{rms} increases with time. However, one should notice that the Stokes number at which N_{rms} reaches the maximum value is not unique at different times. At $T = 12$, the particles with Stokes number of 2 have the highest value of N_{rms}. But at $T = 28$ the particles with Stokes number of 4 have the highest value of N_{rms}. It is well known that the large-scale structures have the most significant effect on the dispersion of the particles when the aerodynamic time scale is of the same order of magnitude as the flow field time scale. From the results of flow field simulation, one knows that the flow field is dominated by the Kelvin–Helmholtz rollers around $T = 12$ and by the pairing of rollers around $T = 28$, and the time scale for the pairing is twice that of the rollup. For this reason the value of N_{rms} peaks at a Stokes number equal to 2 when $T = 12$ and at a Stokes number equal to 4 when $T = 28$.

In order to study the detailed pattern of particle dispersion, a thin slice concept is used here. The plane concept used in the discussion of particle dispersion always corresponds to a thin slice with the thickness of a computational cell. For example, when an (X, Y)-plane at $Z = 0$ is referred to, a thin slice with $0 \leqslant Z < 4\pi/64$ is what it actually means.

4.1. *Effects of two-dimensional large-scale structures*

The different dispersion patterns for the particles at different Stokes numbers can be examined by the distribution of particles in a certain (X, Y)-plane as shown in figure 12. While the particles with small Stokes numbers follow closely the fluid elements, the particles with Stokes numbers of the order of unity tend to accumulate near the circumference of the two-dimensional large structures. The different dispersion

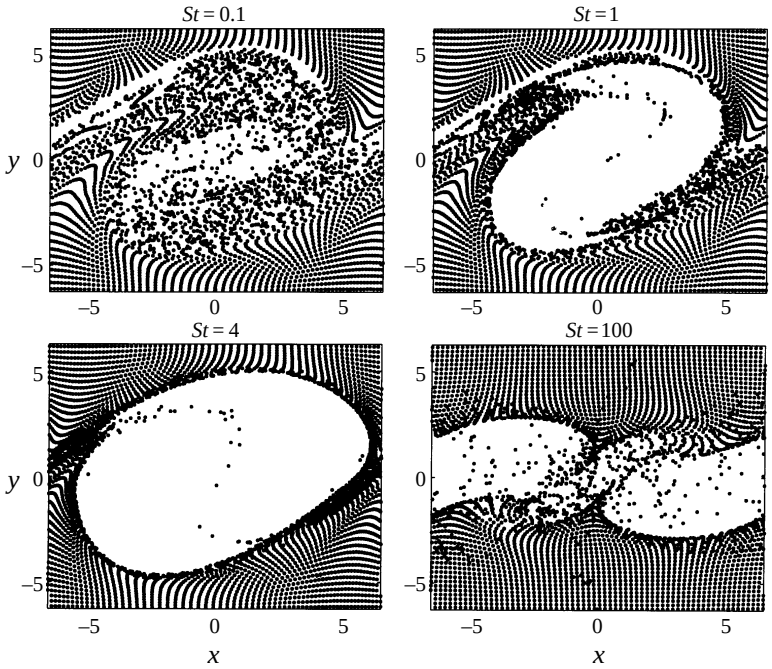

FIGURE 12. Distribution of particles in the $Z = 0$ plane at $T = 28$.

patterns for particles with different orders of Stokes numbers were also found in previous two-dimensional experimental and numerical studies (Chein & Chung 1988; Wen *et al.* 1992). The particles with large Stokes numbers tend to be depleted from the core area of the large structures and accumulate in area of high strain and low vorticity, which is consist with Wen's 'stretching' hypothesis (Wen *et al.* 1992). This trend was also found in a homogeneous turbulent field by Squires & Eaton (1990).

The dispersion patterns for the particles with a Stokes number of 4 at different times are shown in figure 13. The tendency for particles with Stokes number of the order of unity to accumulate at the periphery of the large-scale structures is evident. The re-entry of the spanwise vorticity at $T = 36$ shifts the positions of the maximum particle concentration inward (toward the mid-braid planes).

The root mean square of particle number per cell for each (Y, Z)-plane, $N_{rms}(x)$, is used here to quantify the concentration pattern of particles along the streamwise direction which is mainly governed by the two-dimensional large-scale structures. $N_{rms}(x)$ is obtained from

$$N_{rms}(x) = \left(\sum_{i=1}^{N_{cp}} N_i(x)^2 / N_{cp} \right)^{1/2} \tag{4.2}$$

where N_{cp} is total number of computational cells in one (Y, Z)-plane and $N_i(x)$ is the number of particles in the ith cell in that (Y, Z)-plane. In the present simulation, $N_{cp} = 64 \times 64$.

Figure 14 shows how the particles with different Stokes numbers concentrate along the streamwise direction. The particles with Stokes number equal to 4 have almost the same value of $N_{rms}(x)$ in the middle of the box, but a much larger value of $N_{rms}(x)$ around the mid-braid plane. This shows that the particles with this Stokes number are

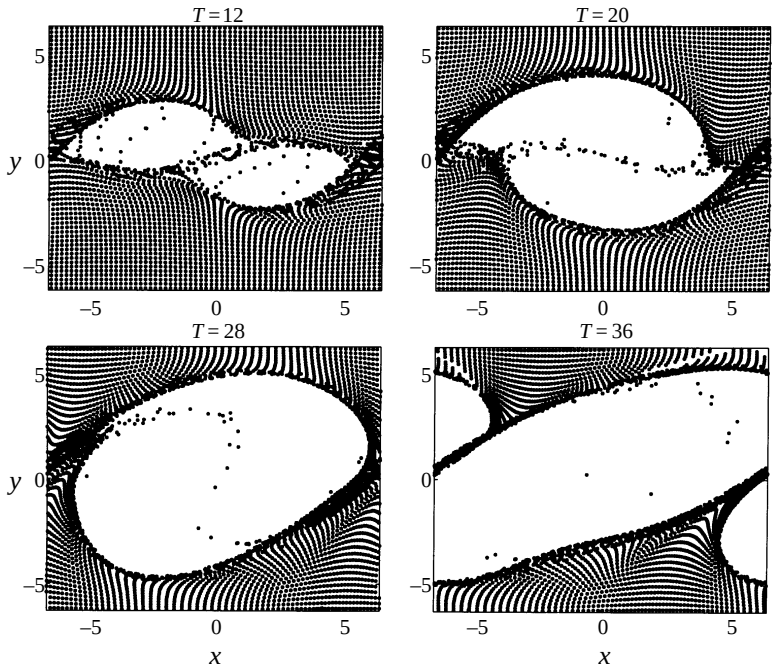

FIGURE 13. Distribution of particles at $St = 4$ in the $Z = 0$ plane.

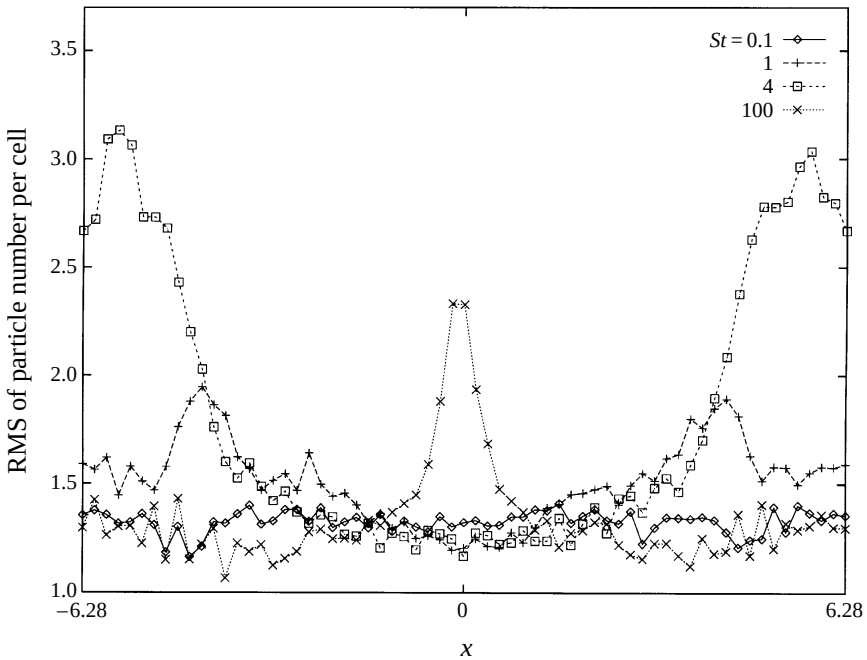

FIGURE 14. $N_{rms}(x)$ for particles with different Stokes number at $T = 28$.

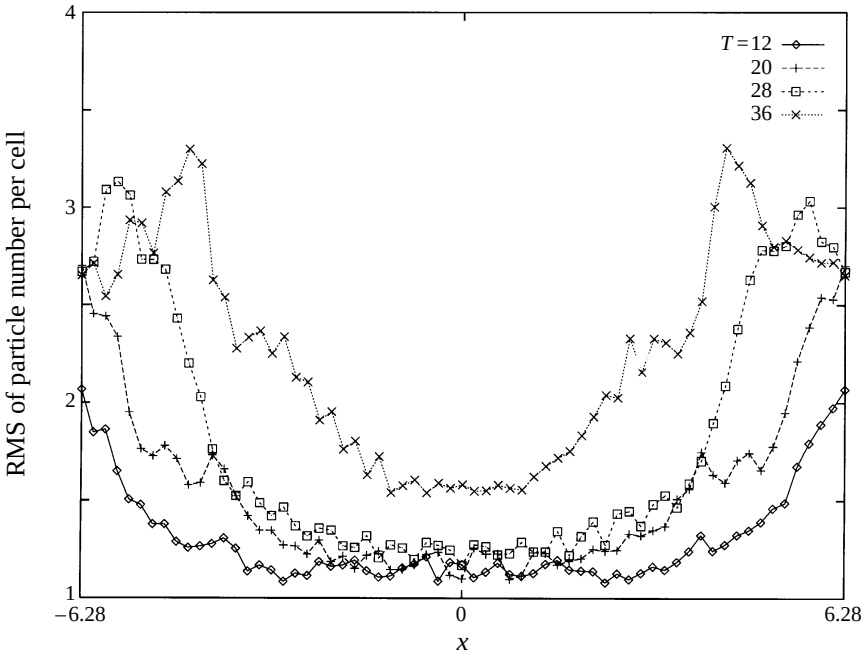

FIGURE 15. $N_{rms}(x)$ for particles with $St = 4$ at different times.

thrown out by the large-scale structures and accumulate around the mid-braid plane. While the concentration of the particles at small Stokes numbers does not vary very much along the streamwise direction, the particles at large Stokes numbers tend to accumulate in the (Y, Z)-plane where the centre of the pairing lies (This (Y, Z)-plane is denoted as the mid-pairing plane.) The difference in $N_{rms}(x)$ for the particles with Stokes number of 4 at different times is shown in figure 15. It is apparent that the level of particle accumulation increases with time, and the positions of the (Y, Z)-planes in which the particles accumulate most move toward the mid-pairing plane.

Another way to quantitatively study the dispersion scales of different particles due to the two-dimensional large-scale vortex is to evaluate the dispersion function in the Y (vertical) direction for particles initially distributed on the $Y = 0$ plane. The dispersion function is defined as

$$D_y(t) = \left(\frac{1}{N_p} \sum_{i=1}^{N_p} (Y_i(t) - Y_m(t))^2 \right)^{1/2} \tag{4.3}$$

where N_p is the total number of particles and $Y_m(t)$ is mean value of particle displacement in the vertical direction at time t. Figure 16 shows the dispersion function of particles with Stokes number ranging from 0.01 to 100. At small time, particles with Stokes number of 0.01 show more dispersion. However, as the time increases, the particles with Stokes number of the order of unity are more dispersed due to the development of large-scale vortex structures and the preferential effect of the structures on particle dispersion. For particles with large Stokes number, the dispersion varies smoothly with T^2. These results are consistent with the two-dimensional result obtained by Chein & Chung (1988).

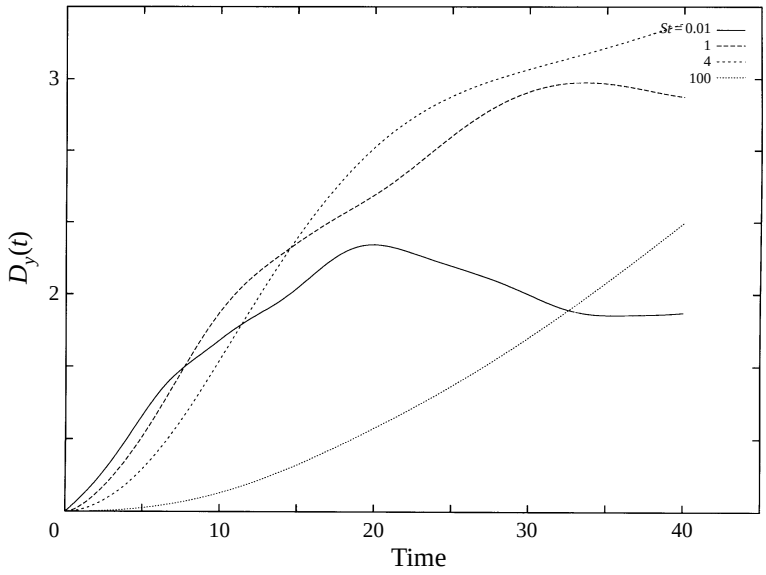

FIGURE 16. Time-dependent particle dispersion in the vertical direction.

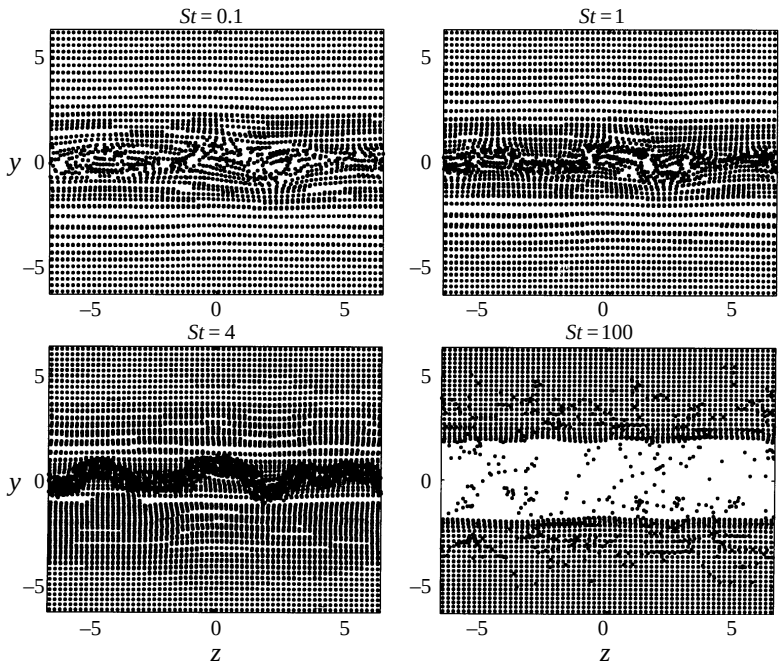

FIGURE 17. Distribution of particles in the mid-braid plane at $T = 28$.

4.2. *Effects of streamwise large-scale structures*

The different dispersion patterns for particles with various Stokes numbers near the mid-braid plane at $T = 28$ is shown in figure 17. At this time, the spanwise vorticity is depleted from the mid-braid region, so the particles accumulate near the $Y = 0$ line due to the effect of the large-scale spanwise vortex structures, except for particles with

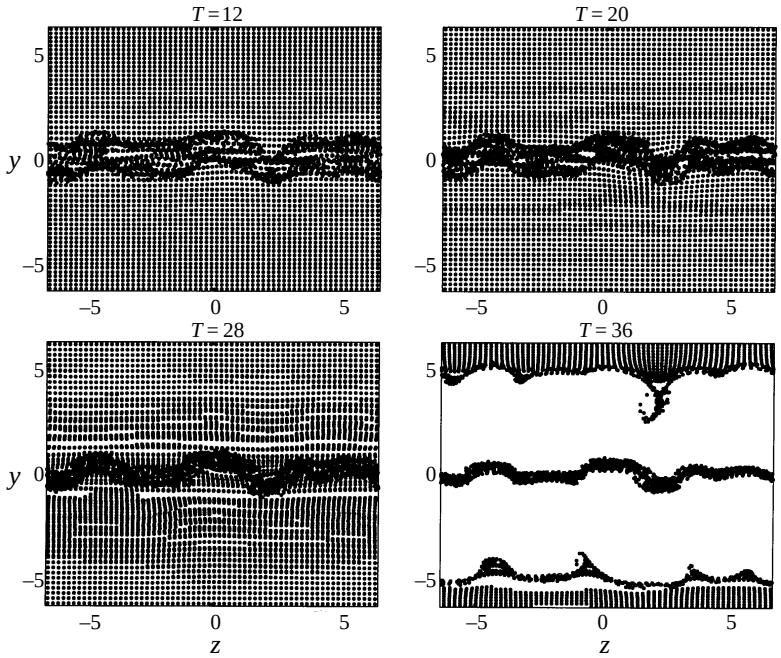

FIGURE 18. Distribution of particles at $St = 4$ in the mid-braid plane.

large Stokes number. For a Stokes number of 4, most of the particles accumulate near the $Y = 0$ line and the streamwise vortices appear to cause the particle concentration to vary along the spanwise direction. Figure 18 shows the dispersion pattern for particles with $St = 4$ near the mid-braid plane at different times. The dispersion pattern at $T = 36$ is caused by both the re-entry of spanwise vorticity and the fully developed streamwise vortices. Typical 'mushroom' structures which are caused by pairs of counter-rotating streamwise vortices are evident here. The 'mushroom' shapes of particle distribution were also observed by Marcu & Meiburg (1996*c*). The 'mushroom' shapes here are not as regular as those in the study of Marcu & Meiburg because the non-forcing three-dimensional perturbation is used here.

When the spanwise vortices first re-enter the mid-braid plane, the strengths of the spanwise and streamwise vortices should be of the same order in the mid-braid plane. Figure 19 shows the effects of the streamwise and spanwise large structures at this time on the dispersion of particles with Stokes number of the order of unity in the mid-braid plane.

Another (Y, Z)-plane used to examine the dispersion pattern of particles is the mid-pairing plane. The different dispersion patterns for particles with different Stokes numbers in this plane are shown in figure 20. As the mid-pairing plane corresponds to the (Y, Z)-plane through the $X = 0$ line in figure 12, it is clear that the particles with Stokes number of the order of unity accumulate most on the circumference of the two-dimensional large structures while the small and large particles distribute more evenly in the (Y, Z)-plane. The variation of the distribution of particles along the Z-axis is due to the streamwise vortices. The dispersion patterns for particles with $St = 4$ in the mid-pairing plane at different times are shown in figure 21. At $T = 12$, the particles are distributed evenly along the Z-direction because the streamwise structure is still developing. With the development of the streamwise structures, the

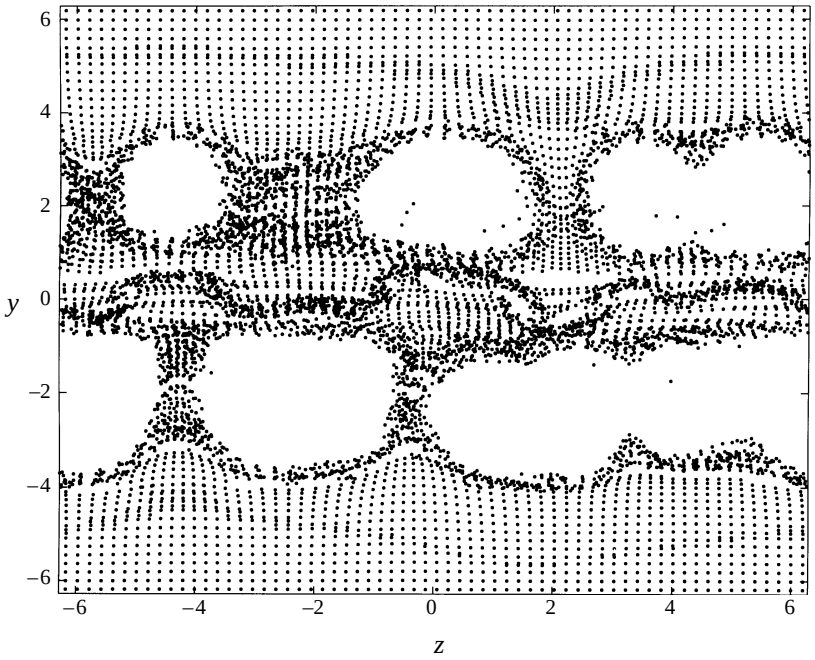

FIGURE 19. Distribution of particles at $St = 3$ in the mid-braid plane at $T = 32$.

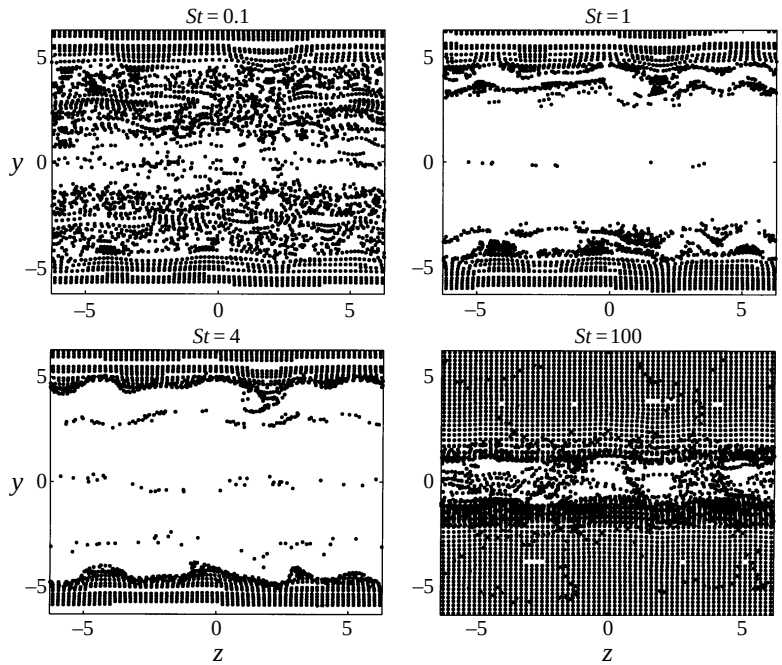

FIGURE 20. Distribution of particles in the mid-pairing plane at $T = 28$.

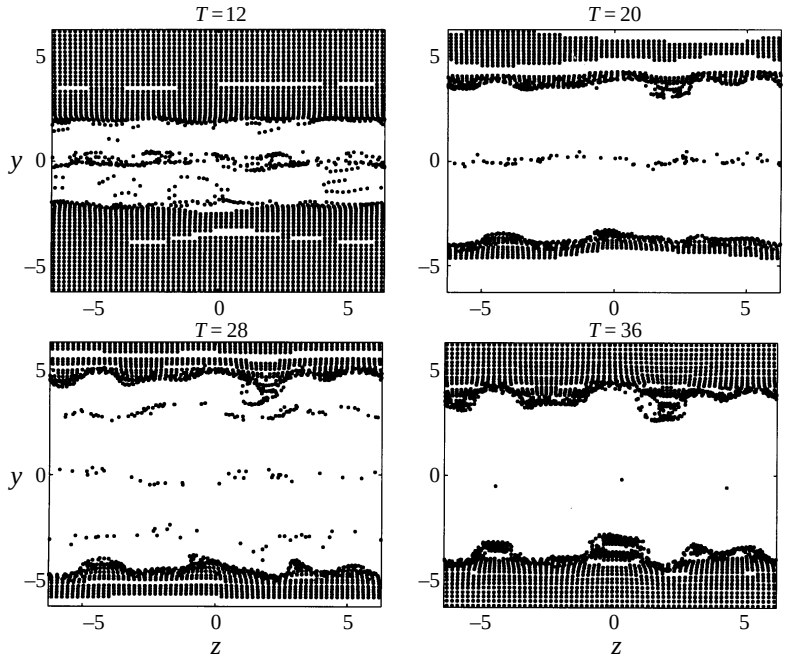

FIGURE 21. Distribution of particles at $St = 4$ in the mid-pairing plane.

variation of particle concentration along the spanwise direction increases and some particles 'burst' out from the high concentration area due to a pair of counter-rotating 'rib' vortices and finally develop a mushroom shaped distribution.

The root mean square of particle number per cell for each (X, Y)-plane, $N_{rms}(z)$, can be used to study the concentration pattern of particles along the spanwise direction. The value of $N_{rms}(z)$ is obtained from

$$N_{rms}(z) = \left(\sum_{i=1}^{N_{cp}} N_i(z)^2 / N_{cp} \right)^{1/2} \tag{4.4}$$

where N_{cp} is the total number of computational cells in one (X, Y)-plane and $N_i(z)$ is the number of particles in the ith cell on that plane.

It is obvious from figure 22 that the variations of the concentration of particles along the spanwise direction for small particles and large particles are minimal, but the variations are much larger for particles with Stokes number of 4 and the variations increase with time as shown in figure 23. The higher concentration for particles with Stokes number of the order of unity in (Y, Z)-plane, which is due to the effect of both two-dimensional large vortex structures and the counter-rotating streamwise vortex structures, was also observed by Marcu & Meiburg (1996*c*)

The dispersion function in the Z (spanwise) direction can be used to quantitatively study the spanwise dispersion scales of different particles which are initially distributed on the $Z = 0$ plane. The function can be defined as

$$D_z(t) = \left(\frac{1}{N_p} \sum_{i=1}^{N_p} (Z_i(t) - Z_m(t))^2 \right)^{1/2} \tag{4.5}$$

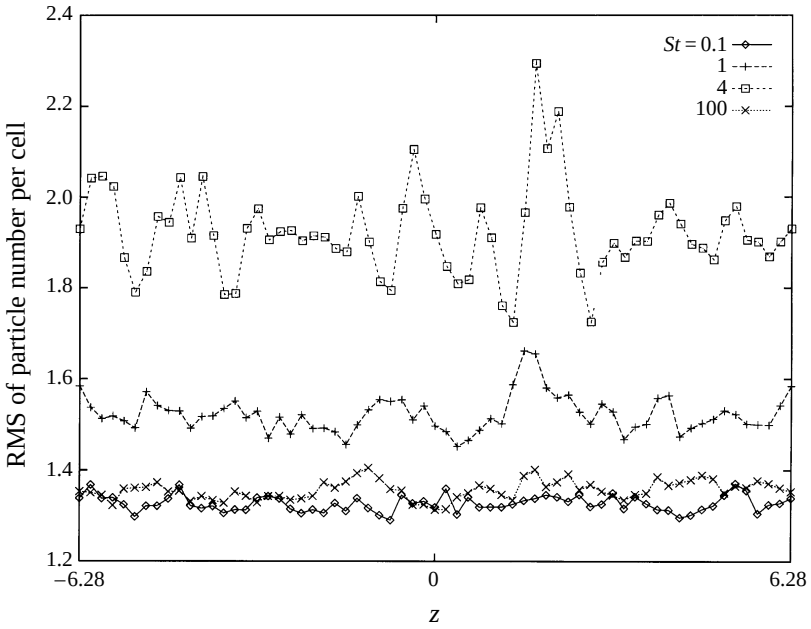

FIGURE 22. $N_{rms}(z)$ for particles at different Stokes number at $T = 28$.

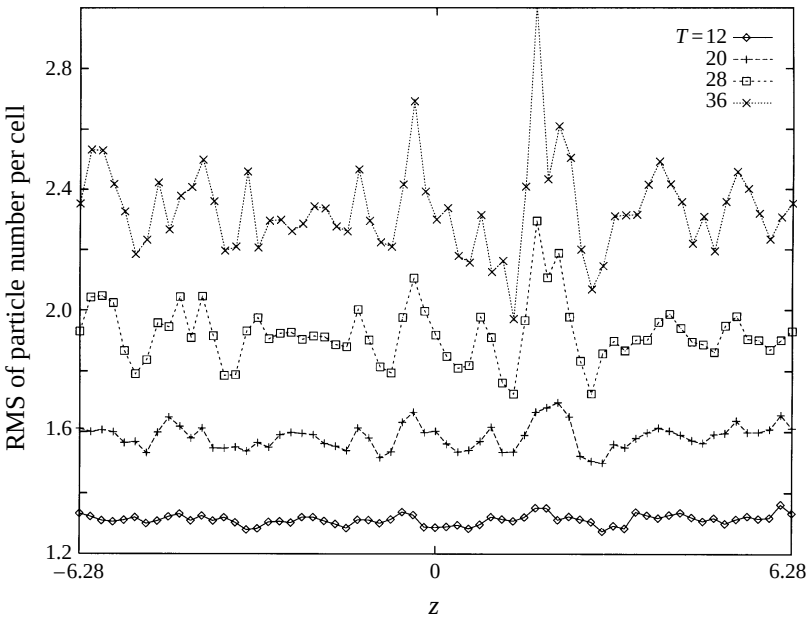

FIGURE 23. $N_{rms}(z)$ for particles at $St = 4$ at different times.

where N_p is the total number of particles and $Z_m(t)$ is the mean value of particle displacement in the spanwise direction at time t. Figure 24 shows that the particles with smaller Stokes number have larger dispersion in the spanwise direction. Compared to figure 16, the dispersion scale in the spanwise direction is much less than that in the vertical direction. This is due to the large difference in the scales of the two-

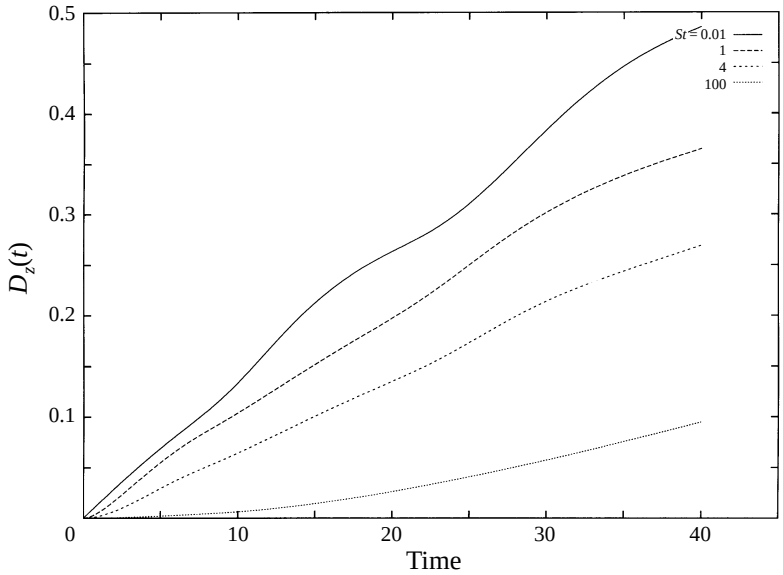

FIGURE 24. Time-dependent particle dispersion in the spanwise direction.

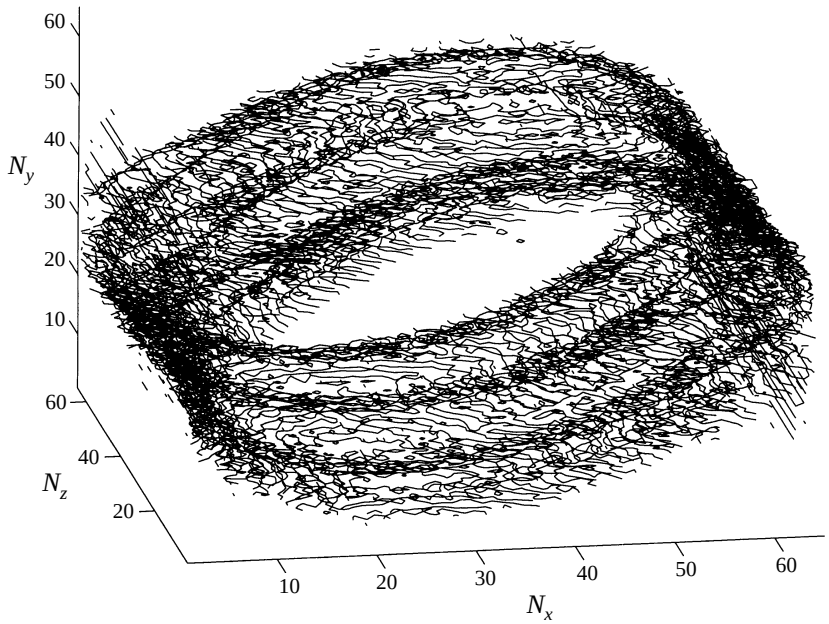

FIGURE 25. Contour plot for when the number of particles per cell is 3 for $St = 4$ at $T = 28$.

and three-dimensional vortices. One should find that there are noticeable waves in the plot of the spanwise dispersion function for particles with small Stokes numbers, probably due to the effects of Kelvin–Helmholtz rollup and pairing.

Figure 25 displays the contour of all the cells where the number of particles in each cell is three for the case of $St = 4$ at $T = 28$ in the entire flow field. It shows how the particles distribute in the entire three-dimensional flow field. The particles concentrate

not only on the circumference of the two-dimensional large-scale structures, but also at some specific positions along the spanwise direction.

5. Conclusions

With a pseudospectral method, the three-dimensional temporally developing mixing layer has been simulated. The time and length scales of the Kelvin–Helmholtz rollup are found to be half those of the pairing of the two adjacent rollers. The simulation shows that the well-known streamwise large-scale structures develop from the initial perturbations and are characterized by the counter-rotating 'rib' vortices, which exist in the braid regions and extend from the bottom of one pairing vortex to the top of the next. The fundamental unstable wavelength in the spanwise direction is also confirmed to be about two thirds of that in the streamwise direction. The pairing has an apparent suppressing effect on the development of the three-dimensionality of the mixing layer and the large-scale streamwise structures can only be fully developed some time after the pairing completes.

The results of particle dispersion show that the dispersion of particles in three-dimensional mixing layers are still mainly dominated by the two-dimensional large-scale structures and that particles with Stokes number of the order of unity tend to concentrate mostly on the circumference of the two-dimensional large-scale structures. Owing to the different time scales of the rollup and the pairing, the Stokes numbers at which the particles concentrate most are different at the rollup time and the pairing time. However, the effect of the streamwise large-scale structures on the dispersion of particles is noticeable and increases with the development of the three-dimensionality of the mixing layer. While the two-dimensional large-scale structures move the particles at certain Stokes numbers towards the circumference of the structures, a pair of counter-rotating 'rib' vortices can transport the particles in or out the two-dimensional large vortex structures which results in the mushroom shape of the particle distribution.

The authors would like to thank Professor Jim Riley of the University of Washington and Dr. Pat McMurtry who provided the initial version of the computational program. The authors also want to thank Dr. Rogers and Dr. Moser for sending some results of their work. The authors gratefully acknowledge the support of Department of Energy Grant No. DE-FG06-94ER-14450 under the direction of Dr. Oscar Manley and Dr. Robert Goulard.

Appendix. Three-dimensional perturbation specifications

First, a three-dimensional isotropic energy spectrum is specified on low wavenumbers:

$$E_u(k) = \varepsilon_{3D} \frac{k^2 \Lambda^3}{(1 + k^2 \Lambda^2)^3} \tag{A 1}$$

where k is the magnitude of the wavenumber vector $\boldsymbol{k}$, Λ is a integral length scale and ε_{3D} determines the level of the perturbations. The energy spectrum is related to a stream function $\Psi(\boldsymbol{x})$ by following steps:

(i) obtain $E_\psi(k)$ by $E_\psi(k) = \frac{2}{3}k^2 E_u(k)$,

(ii) obtain $\psi(k)$ by $\psi(k) = [(\Delta k / N(k)) E_\psi(k)]^{1/2}$,

(iii) obtain $\Psi(\boldsymbol{k})$ by adding a random phase to each $\boldsymbol{k}$ of $\psi(k)$,

(iv) transfer $\Psi(\boldsymbol{k})$ from spectral space to physical space to get $\Psi(\boldsymbol{x})$,

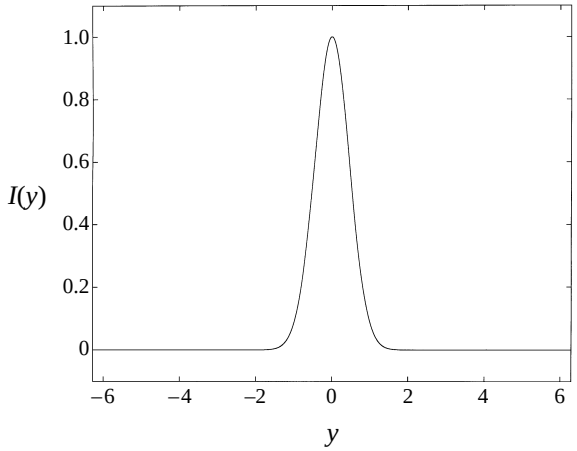

FIGURE 26. Profile of the form function $I(y)$.

where $N(k)$ is the number of modes between wavenumber k and $k + \Delta k$. Finally, an incompressible velocity field is obtained from the stream function:

$$\boldsymbol{U}(\boldsymbol{x}) = \nabla \times (I(y)\Psi(\boldsymbol{x})) \tag{A 2}$$

where $I(y)$ is a form function used to specify a chosen r.m.s. profile (figure 26) of the fluctuating velocity.

REFERENCES

BREIDENTHAL, R. E. 1978 A chemically reacting turbulent shear layer. PhD thesis, California Institute of Technology.

BREIDENTHAL, R. E. 1981 Structure in turbulent mixing layers and wakes using a chemical reaction. *J. Fluid Mech.* **109**, 1–24.

BROWAND, F. K. & TROUTT T. R. 1980 A note on spanwise structure in the two-dimensional mixing layer. *J. Fluid Mech.* **97**, 771–781.

CHEIN, R. & CHUNG, J. N. 1988 Simulation of particle dispersion in a two-dimensional mixing layer. *AIChE J.* **34**, 946–954.

CROWE, C. T., CHUNG, J. N. & TROUTT, T. R. 1988 Particle mixing in free shear flows. *Prog. Energy Combust. Sci.* **14**, 171–194.

CROWE, C. T., TROUTT, T. R. & CHUNG, J. N. 1996 Numerical models for two-phase turbulent flows. *Ann. Rev. Fluid Mech.* **28**, 11–43.

EATON, J. K. & FESSLER, J. R. 1994 Preferential concentration of particles by turbulence. *Intl J. Multiphase Flow* **20**, 169–209.

ELGHOHASHI, S. E. 1994 On predicting particles by turbulence. *Appl. Sci. Res.* **52**, 309–329.

HO, C.-M. & HUERRE P. 1984 Perturbed free shear layers. *Ann. Rev. Fluid Mech.* **16**, 365–424.

HUANG, L.-S. & HO, C.-M. 1990 Small-scale transition in a plane mixing layer. *J. Fluid Mech.* **290**, 475–500.

ISHII, R., UMEDA, Y. & YUHI, H. 1989 Numerical analysis of gas-particle two-phase flows. *J. Fluid Mech.* **207**, 475–515.

LASHERAS, J. C., CHO, J. S. & MAXWORTHY, T. 1986 On the origin and evolution of streamwise vortical structures in a plane free shear flow. *J. Fluid Mech.* **172**, 231–258.

LASHERAS, J. C. & CHOI, H. 1988 Three-dimensional instability of a plane free shear layer: an experimental study of the formation and evolution of streamwise vortices. *J. Fluid Mech.* **189**, 53–86.

MARCU, B. & MEIBURG, E. 1996*a* The effect of streamwise braid vortices on the particle dispersion in a plane mixing layer. I. Equilibrium points and their stability. *Phys. Fluids* **8**, 715–733.

MARCU, B. & MEIBURG, E. 1996*b* The effect of streamwise braid vortices on the particle dispersion in a plane mixing layer. II. Nonlinear particle dynamics. *Phys. Fluids* **8**, 734–753.

MARCU, B. & MEIBURG, E. 1996*c* Three-dimensional features of particle dispersion in a niminally plane mixing layer. *Phys. Fluids* **8**, 2266–2268.

MCMURTRY, P. A., RILEY, J. J. & METCALFE, R. W. 1989 Effect of heat release on the large-scale structure in turbulent mixing layer. *J. Fluid Mech.* **199**, 297–332.

METCALFE, R. W., ORSZAG, S. A., BRACHET, M., MENON, S. & RILEY, J. J. 1987 Secondary instability of a temporally growing mixing layer. *J. Fluid Mech.* **184**, 207–243.

MICHALKE, A. 1964 On the inviscid instability of the hyperbolic tangent velocity profile. *J. Fluid Mech.* **19**, 543–556.

MIKSAD, R. W. 1972 Experiments on the nonlinear stages of free shear layer transition. *J. Fluid Mech.* **56**, 695–719.

MOSER, R. D. & ROGERS, M. M. 1993 The three-dimensional evolution of a plane mixing layer: pairing and transition to turbulence. *J. Fluid Mech.* **247**, 275–320.

PEYRET, R. & TAYLOR, T. D. 1983 *Computational Methods for Fluid Flow*. Springer.

PIERREHUMBERT, R. T. & WIDNALL, S. E. 1982 The two- and three-dimensional instabilities of a spatially periodic shear layer. *J. Fluid Mech.* **114**, 59–82.

SQUIRES, K. D. & EATON, J. K. 1990 Particle response and turbulence modification in isotropic turbulence. *Phys. Fluids* A **2**, 1191–1203.

SQUIRES, K. D. & EATON, J. K. 1991*a* Lagrangian and Eulerian statistics obtained from direct numerical simulation of homogeneous turbulence. *Phys. Fluids* A **3**, 130–143.

SQUIRES, K. D. & EATON, J. K. 1991*b* Preferential concentration of particles by turbulence. *Phys. Fluids* A **3**, 1169–1178.

SQUIRES, K. D. & EATON, J. K. 1991*c* Measurements of particle dispersion obtained from direct numerical simulation of isotropic turbulence. *J. Fluid Mech.* **226**, 1–35.

WANG, L. P. & MAXEY, M. R. 1993 Settling velocity and concentration distribution of heavy particles in homogeneous turbulence. *J. Fluid Mech.* **256**, 27–68.

WEN, F., KAMALU, N., CHUNG, J. N., CROWE, C. T. & TROUTT, T. R. 1992 Particle dispersion by vortex structure in plane mixing layers. *Trans. ASME*: *J. Fluids Engng* **114**, 657–666.

WYGNANSKI, I., OSTER, D., FIEDLER, H. & DZIOMBA, B. 1979 On the perseverance of a quasi-two-dimensional eddy-structure in a turbulent mixing layer. *J. Fluid Mech.* **93**, 325–336.

YEUNG, R. K. & POPE, S. B. 1988 An algorithm for tracking particles in numerical simulations of homogeneous turbulence. *J. Comput. Phys.* **79**, 373–416.